33RD CONGRESS
OF THE INTERNATIONAL COUNCIL
OF THE AERONAUTICAL SCIENCES
STOCKHOLM, SWEDEN, 4-9 SEPTEMBER, 2022

ICAS 2022 SWEDEN

COMPUTATIONAL ANALYSIS OF SUPERSONIC FLOW AROUND A WEDGE AND A CYLINDER USING BUILDING-CUBE METHOD

Kumpei Abe[1], Sayaka Miyazaki[1], Daisuke Sasaki[1], Shun Takahashi[2] & Gohji Yamada[2]

[1] Kanazawa Institute of Technology
[2] Tokai University

Abstract

A Cartesian-mesh CFD coupled with immersed boundary method was applied to solve supersonic flows with heat transfer around a circular cylinder and a wedge. The results of pressure profiles were matched with the structured mesh CFD for both cases. The wall heat flux for a cylinder agrees well with the reference, while discrepancy is observed for a wedge.

Keywords: Supersonic, Cartesian Mesh, Building-Cube Method (BCM), Aerodynamic heating

1. Research background and objective

In 2021, United Airlines announced that it would conditionally purchase a supersonic airliner. Virgin Galactic founder Sir. Branson successfully made a space flight on the spacecraft “VSS Unity” on July 11, 2021. In the next-generation space transport industry, winged spaceplanes are once again in the spotlight. On the basis of these events, it is presumed that the development of supersonic and hypersonic aircraft has been actively carried out in recent years. However, supersonic and hypersonic aircrafts have many problems that must be solved, such as noise and another environmental compatibilities, and economic problems. In addition, one of the serious problems is the shock waves or shock wave interference, which may cause serious damage to an airframe.

In recent years, a lot of research have been conducted on aerodynamic simulation using Cartesian Mesh CFD in the subsonic and transonic regions due to the ease of application to the actual sharp of the aircraft frame [1,2]. At Japan Aerospace Exploration Agency (JAXA), a Cartesian Mesh-based CFD Workshop was held to discuss the applicability of Cartesian Mesh CFD for supersonic and hypersonic flows including heat transfer [3]. Because a geometry surface is represented by a stair step for Cartesian mesh, it causes difficulty in boundary representation. In addition, it is also difficult to precisely predict boundary layer and heat transfer.

In this study, Immersed Boundary Method (IBM) is modified to compute wall heat flux with shock waves on the Cartesian mesh. The calculations in this study are carried out using the Building-Cube Method (BCM) solver with isothermal walls imposed. The computational target is a blunt body and a sharp body: a circular cylinder and a wedge. A circular cylinder is chosen as a blunt body to compute pressure and temperature distribution with bow shock wave. On the other hand, oblique shock is generated around a wedge or a sharp body. Similarly, the pressure and temperature distribution around the wedge is computed using BCM. The computational results are compared with structured-mesh CFD results for the validation. The purpose of the study is to examine the applicability of the BCM with IBM implemented to supersonic flows including heat transfer through the computations.

2. Method

2.1 Building-Cube-Method

This study adopts the BCM which is based on the block-structured Cartesian mesh [4]. The BCM divides the computational domain into many blocks (or subdomains) that are called “Cube”. Then, equally spaced Cartesian meshes that are called “Cell” are filled in Cubes. The computational domain is composed of many Cubes (blocks) of different sizes, but they have the same number of Cells regardless of the Cube size. Thus, the computational effort for each Cube is ideally identical regardless of the Cube, which has a great advantage in parallel computations.

2.2 Immersed Boundary Method for adiabatic wall

As stated above, the surface of an object’s is represented by a staircase shape. Immersed Boundary Method (IBM) [5] using Ghost Cell (GC) and Image Point (IP) [6] are used for the wall boundary condition. As shown in Figure 1, the Cell adjacent to the Fluid Cell is defined as GC and the point located 1.5 times the minimum cell size in the normal direction from the surface of the object is defined as IP [7]. In the 2D simulation, the physical quantities at IP is computed by inverse distance weighted interpolation in Equation 1 from the nine points surrounding the IP. For the GC, pressure p_{GC} is given as in Equation 2. Velocity U_{GC} is given to maintain that the velocity is zero on the surface of the object using Equation 3.

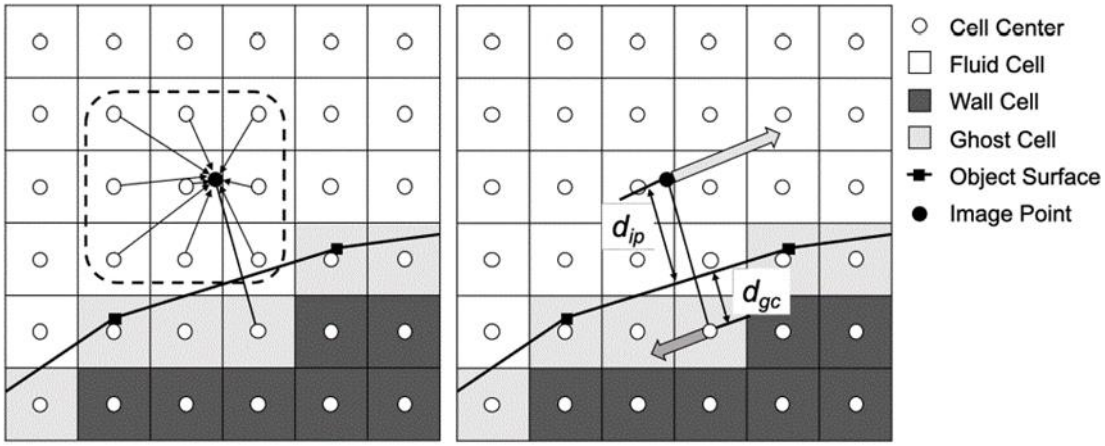

Figure 1 Immersed Boundary Method with Ghost Cell

$$Q_{IP} = \frac{\sum_{i=1}^{9} w_i Q_i}{\sum_{i=1}^{n} w_i} \qquad w_i = \frac{1}{\sqrt{(x - x_i)^2 + (y - y_i)^2}} \tag{1}$$

$$p_{GC} = p_{IP} \tag{2}$$

$$U_{GC} = -\frac{d_{GC}}{d_{IP}} U_{IP} \tag{3}$$

$$\rho_{GC} = \rho_{IP} \tag{4}$$

2.3 Immersed Boundary Method for isothermal wall

According to the given wall surface temperature, the density in GC is calculated from the wall surface temperature. Since the density at IP is computed using Fluid Cell, the temperature is computed from IP and GC, and a temperature gradient is then computed. The wall heat flux is predicted using the temperature gradient. To obtain the heat flux near the object, an isothermal wall boundary condition is imposed on the object. To impose the isothermal condition, it is necessary to define a temperature gradient in the vicinity of the object. Temperature gradient is defined on the line between IP and GC as shown in Figure 2. To compute the gradient, a surface wall temperature T_w is set on the object surface in Figure 2 and the density on the object surface is obtained from the following Equation 5.

The density is substituted into the GC and the calculation is carried out.

$$\rho_{IB} = \frac{\gamma}{\gamma - 1}\frac{p_{IP}}{T_{IB}C_p} \tag{5}$$

The heat flux q is calculated using Equation 6, where κ is the specific heat ratio and Δx is minimum cell size.

$$q = \kappa\frac{T_{IP} - T_w}{0.5\Delta x} \tag{6}$$

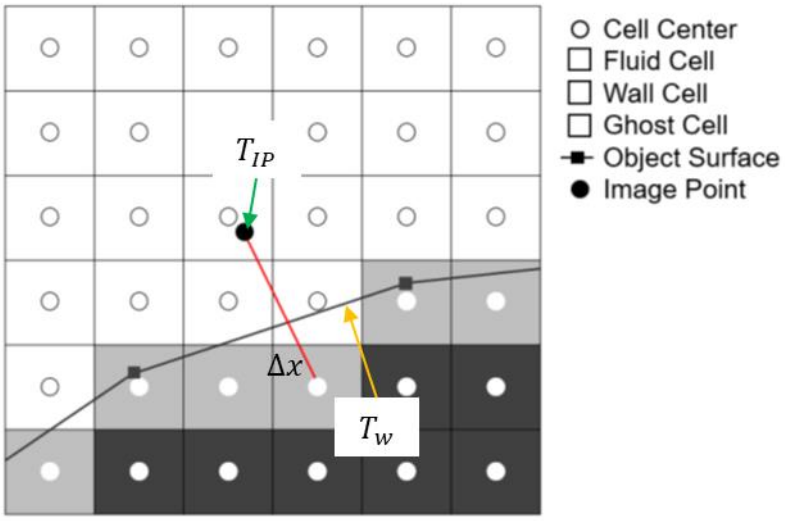

Figure 2 Immersed Boundary Method for temperature gradient

2.4 Computational conditions

Table 1 shows the computational schemes used in this study. Table 2 summarizes the computational conditions and mesh information for a circular cylinder, and Table 3 summarizes the conditions and mesh information for a wedge. Figures 4 and 5 show mesh diagrams around a cylinder and a wedge generated by BCM GridGene [8]. Three types of mesh resolution are defined, called fine, medium, and coarse, in descending order of minimum cell size.

Table 1 Computation Method

Governing Equation	2D Compressible Navier-Stokes equations
Inviscid flow evaluation	HLLEW
High-order accuracy method	Third-order accuracy MUSCL
Viscous flux evaluation	Second-order accuracy central difference
Time integration method	LU-SGS implicit method
Turbulence model	Spalart-Allmaras model
Wall boundary	IBM with GC and IP

Table 2 Computational conditions for Cylinder

(a) Computation condition

Mach number (M)	[-]	3.0
Reynolds number (Re)	[-]	10^3, 10^4, 10^5
Standard Temperature (T_{inf})	[K]	215
Wall Temperature (T_w)	[K]	215
Standard Pressure (P_{inf})	[Pa]	0.72
Specific heat ratio (γ)	[-]	1.4
Diameter (D)	[m]	0.001

(b) Mesh information

		Fine	Medium	Coarse
Minimum Cell size	[m]	$2.38\times10^{-5}D$	$1.94\times10^{-4}D$	$3.81\times10^{-4}D$
Outer size	[m]	$50D\times50D$		
Number of Cube		19,081	2,644	1,405
Division of Cube		32×32		
Number of Cell		19,538,944	2,707,456	1,438,720

Table 3 Computational conditions for Wedge

(a) Computation condition

Mach number (M)	[-]	5.0
Reynolds number (Re)	[-]	10^5
Standard Temperature (T_{inf})	[K]	333
Wall Temperature (T_w)	[K]	300
Standard Pressure (P_{inf})	[Pa]	1047.7
Specific heat ratio (γ)	[-]	1.4
Representative length (L)	[m]	0.1
Wedge angle (α)	[deg]	15

(b) Mesh information

		Fine	Medium	Coarse
Minimum Cell size	[m]	$2.38\times10^{-5}L$	$4.77\times10^{5}L$	$1.91\times10^{-4}L$
Outer size	[m]	$50L\times50L$		
Number of Cube		14,258	7,232	2,190
Division of Cube		32×32		
Number of Cell		14,600,192	7,405,568	2,242,560

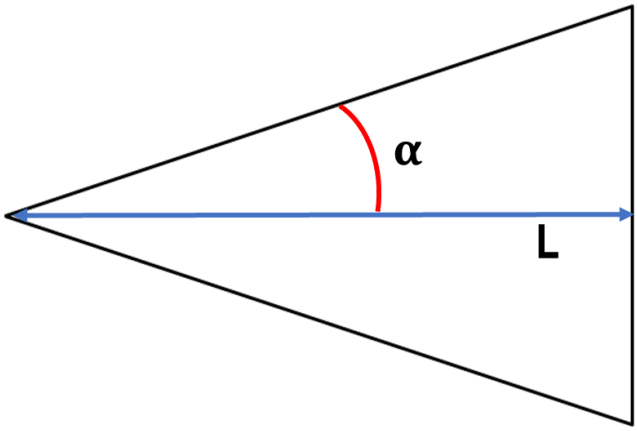

Figure 3 Wedge model

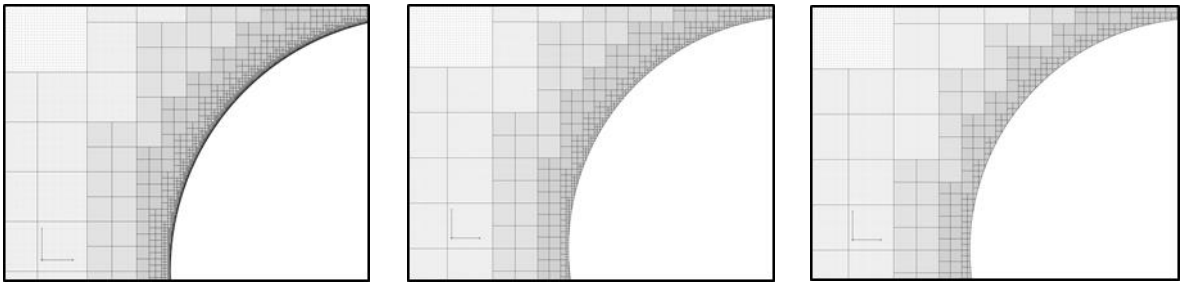

(a) Fine (b) Medium (c) Coarse

Figure 4 Mesh near the Cylinder

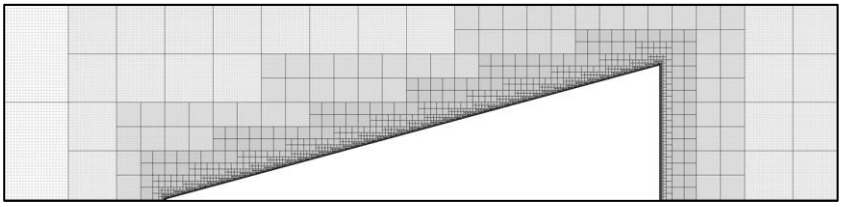

(a) Fine

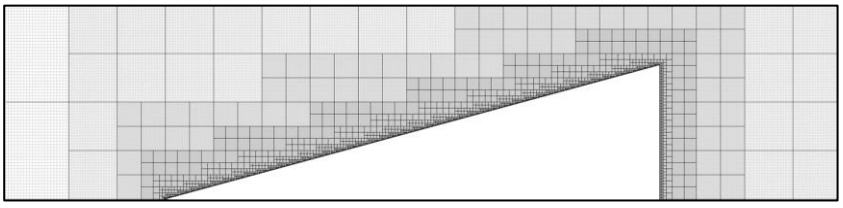

(b) Medium

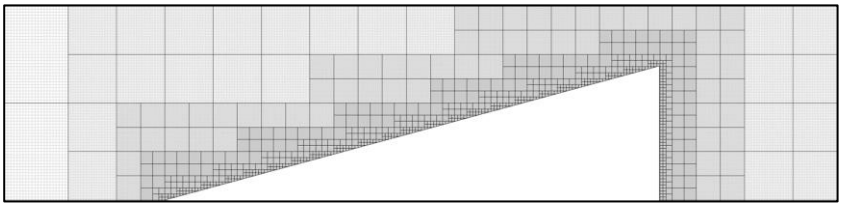

(c) Coarse

Figure 5 Mesh near the Wedge

3. Circular cylinder result

3.1 Comparison of isothermal and adiabatic walls

Firstly, computational results of isothermal wall boundary conditions and conventional adiabatic wall boundary conditions are compared. In this comparison, the Reynolds number (*Re*) is set to 10^5 and medium mesh are employed. A visualization of the pressure coefficients is shown in Figure 6. The visualization shows that there are no differences in the distributions and that the calculations are similar regardless of the types of walls. The surface pressure coefficients for each wall surface are plotted in Figure 7. The result of the CFD of the structured mesh [3] is also plotted for comparison. The graphs also show that both the isothermal and adiabatic walls have the same distribution, which is in good agreement with the structured mesh results

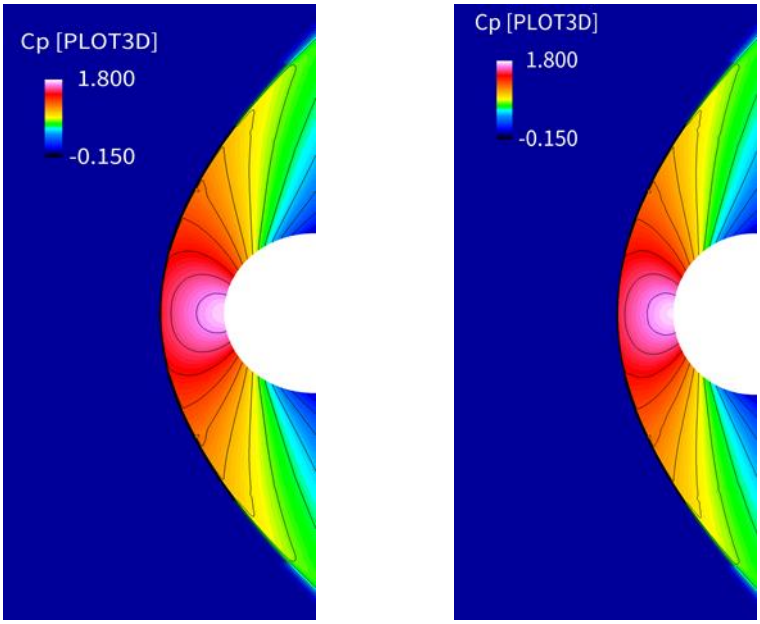

(a) isothermal wall (b) Adiabatic wall

Figure 6 Visualization of *Cp* (isothermal VS adiabatic wall)

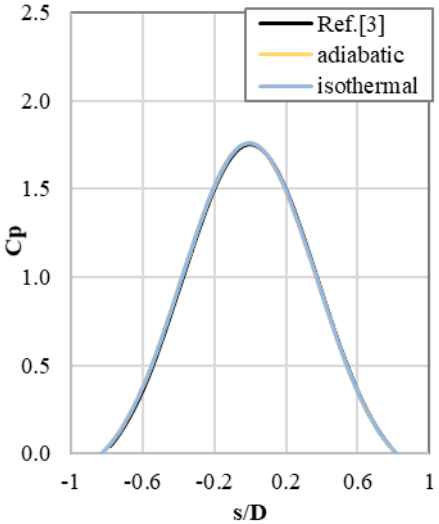

Figure 7 Surface pressure coefficient (isothermal VS adiabatic wall)

3.2 Mesh Dependency

The computational results for different mesh resolution are compared. The visualization of the pressure coefficient at Re=10^5 and M=3.0 is shown in Figure 8. The visualization shows that there is no difference between the mesh and that the mesh has similar values and distribution trends. Furthermore, the surface pressure coefficients for three different Reynolds numbers (Re=10^3, 10^4, 10^5) are compared in Figure 9, respectively. The surface pressure coefficients show no significant differences in any mesh, and the distributions are matched with structured mesh CFD. It is indicated that the present Cartesian mesh CFD can be used to calculate the shock waves and the pressure component with sufficient accuracy.

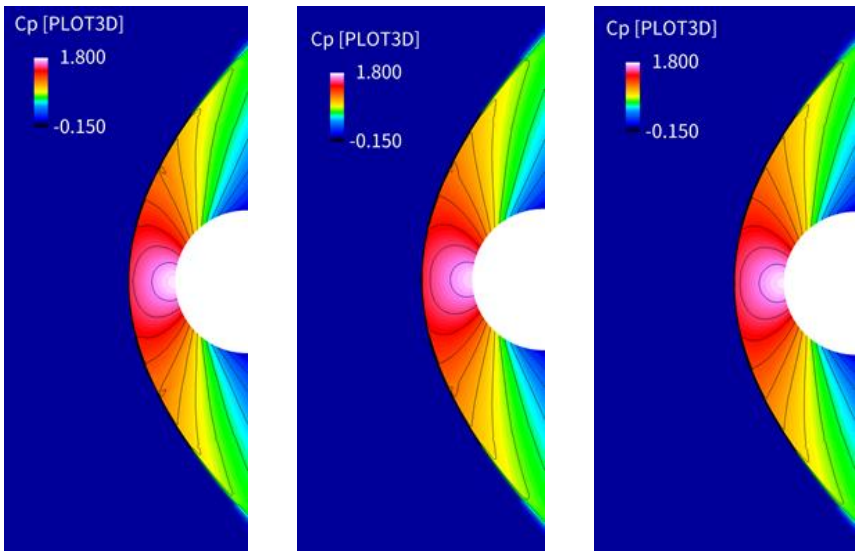

(a) Fine (b) Medium (c) Coarse

Figure 8 Visualization of *Cp* (*Re*10^5)

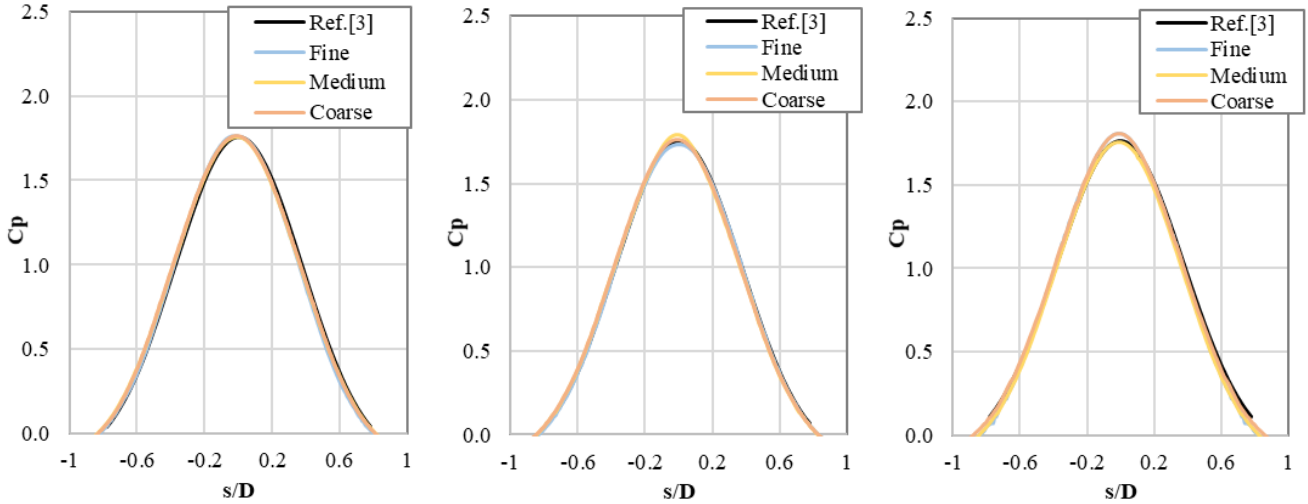

(a) *Re*10^5 (b) *Re*10^4 (c) *Re*10^3

Figure 9 Surface pressure coefficient, *Cp*

3.3 Stream distribution at stagnation point

In this section, the temperature distribution is computed for different Reynolds numbers at the fixed Mach number M=3. A visualization of the temperature field for medium mesh is shown in Figure 10. Figure 10 reveals that the temperature boundary layer becomes thicker as the Reynolds number decreases for the same Mach number. Figure 11 shows the temperature change and shock wave

stand-off distance of the shock wave from the stagnation point. The temperature change near the stagnation point is clearly shown by the thickness of the temperature boundary layer in the difference in Reynolds number. Although there are slight variations in the values according to mesh resolution, they are all within 8% errors compared to the CFD results of the structured mesh CFD. However, at Re=10^5, some oscillations were observed between the surface of the object and the shock wave.

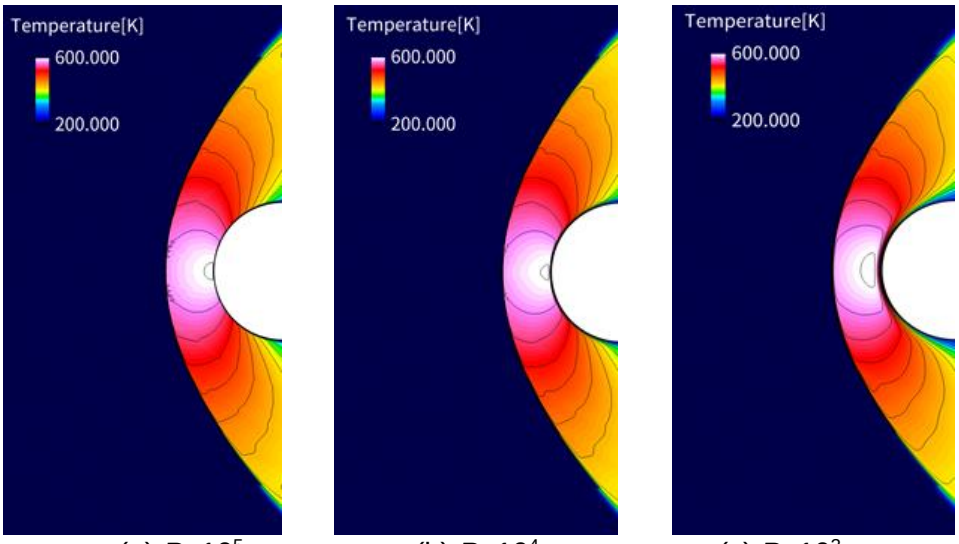

(a) $Re10^5$ (b) $Re10^4$ (c) $Re10^3$

Figure 10 Temperature (Medium Mesh)

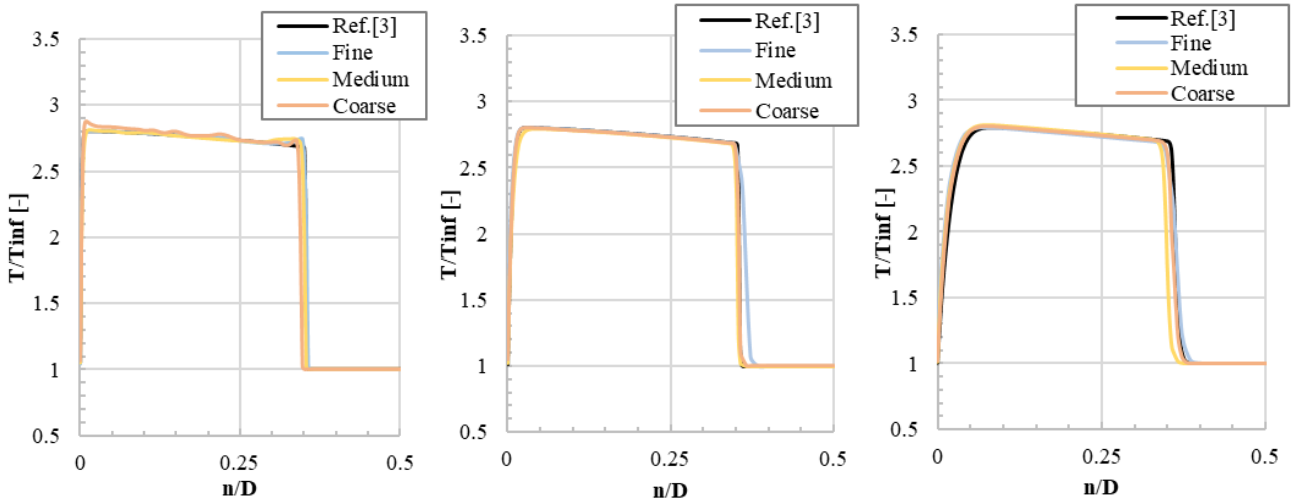

(a) $Re10^5$ (b) $Re10^4$ (c) $Re10^3$

Figure 11 Temperature distribution from stagnation to shock wave location

3.4 Heat flux distribution

The wall heat flux obtained from the present computation is shown in Figure 12. In general, the heat flux distribution around a circular cylinder is known to be a parabolic distribution with a maximum value at the stagnation point. The fine mesh results of Re=10^5 show a parabolic distribution similar to structured mesh CFD. The maximum heat fluxes on the medium and coarse mesh were small compared to the reference. The maximum heat flux on the Re=10^3 case reaches an overestimation. This suggests that there is a difference in the minimum mesh size required to calculate the heat flux distribution for different Reynolds numbers. To investigate the relationship between the minimum mesh size and the Reynolds number, the cell Reynolds number Rc was calculated and is summarized

in Table 4. The cell Reynolds number is obtained from the following Equation 7.

$$R_c = \frac{\rho M c}{\mu} \tag{7}$$

$$\text{c: } minimum\ cell\ size$$

In general, it is recommended that *Rc*=1 is required to accurately solve the heat flux. For mesh satisfying *Rc*=1, the distribution trend can be captured comparatively well, and the values are close to those of reference. However, it was confirmed that the heat flux distribution was not fully captured on the mesh, which do not correspond to the mesh size mentioned above. Thus, the cell Reynolds number *Rc* can be an indicator of the accuracy of the heat flux in this analysis. Brahmachary also presented the phenomenon that the maximum heat flux oscillates at the peak in the analysis using the embedded boundary method of the Ghost-Cell based approach [9].

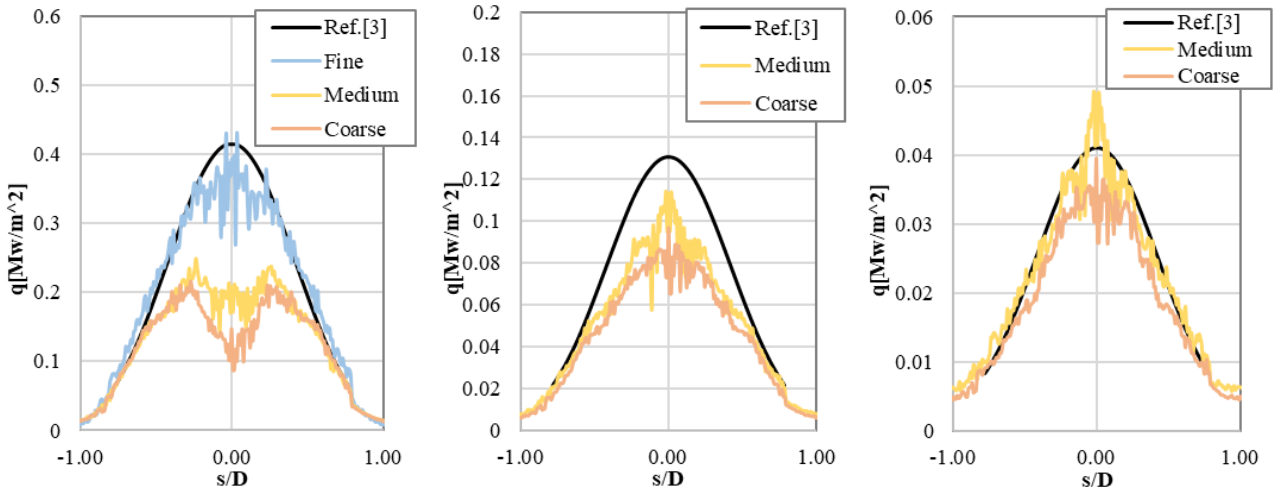

(a) *Re*10^5 (b) *Re*10^4 (c) *Re*10^3

Figure 12 Heat flux

Table 4 Difference in Cell Reynolds Number

	Fine	Medium	Coarse
***Re*10^5**	2.367	19.3	37.9
***Re*10^4**	0.237	1.93	3.79
***Re*10^3**	0.0237	0.193	0.379

4. Wedge Result

4.1 Pressure distribution

Pressure distribution Figure 13 shows a visualization of the non-dimensionalized pressure distribution around a wedge at M=5 and Re=10^5. The visualization shows that there are no significant difference in pressure distribution for all mesh cases. According to the definition of coordinates shown in Figure 14, the spatial pressure distribution along the coordinate near plotted in Figure 15. Figure 15 (b) and (a) show the pressure distributions at the different locations. The pressure distributions show that the location of shock wave is quite matched for all cases, while the slight discrepancy is observed for coarser mesh cases. The discrepancy at the compression region of BCM results with the structured mesh results at is considered to be largely due to the mesh resolution.

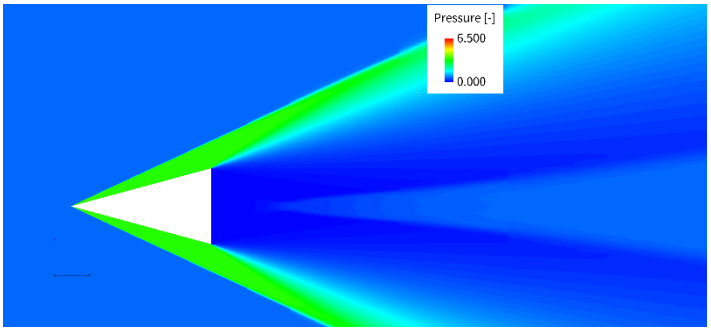

(a) Fine

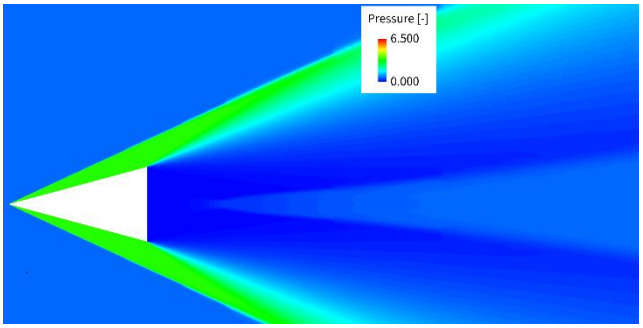

(b) Medium

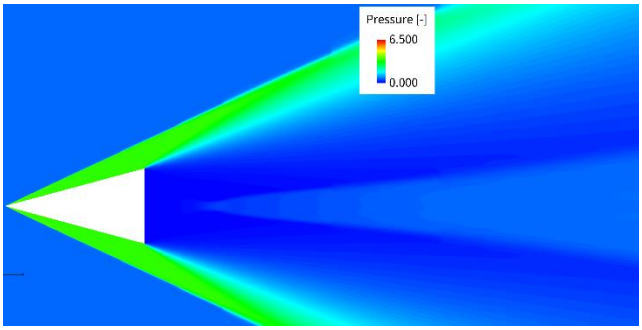

(c) Coarse

Figure 13 Nondimensionalized pressure distribution visualization diagram

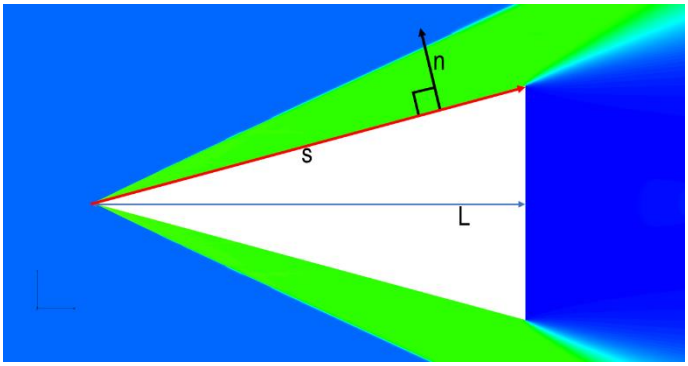

Figure 14 Definition of a wedge

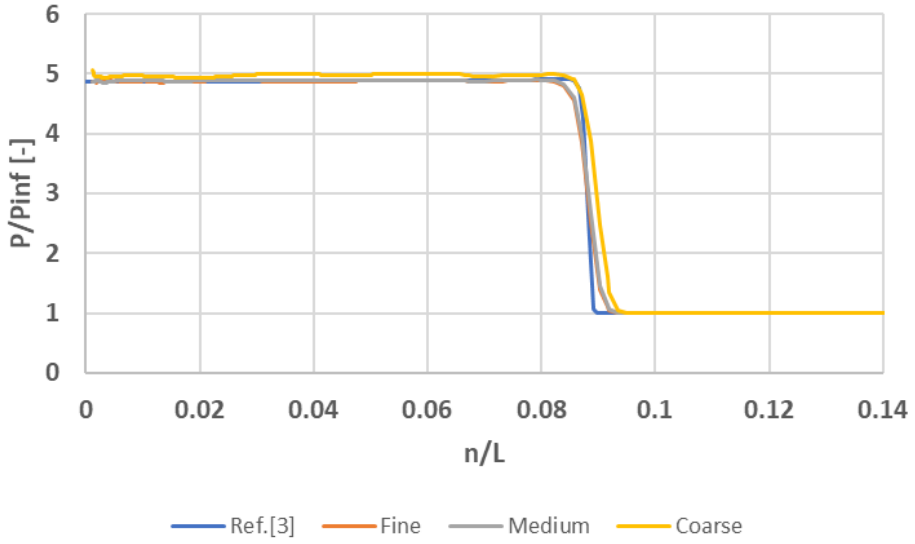

(a)0.5*L*

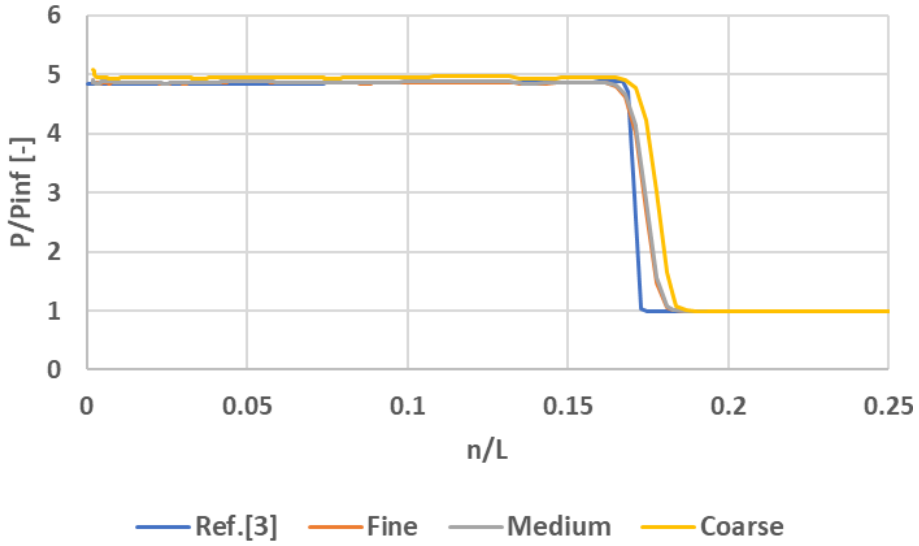

(b)1.0*L*

Figure 15 Pressure distribution

4.2 Temperature distribution

Temperature distribution Figure 16 shows a visualization of the non-dimensionalized temperature contours for boundary condition pf the isothermal wall. The visualization shows that there is no significant difference in the temperature distribution for any mesh size. Figure 17 shows the temperature distribution calculated along the defined coordinate n. The temperature distribution of coarse mesh is overestimated compared to other results as a whole. It seems that the overall temperature distributions of medium and fine mesh are similar to the results of structured mesh. Figure 18 shows the heat flux distribution near the wedge. The heat flux values of medium and fine mesh are 10 times larger compared to results of the structured mesh. This is due to the difference of the temperature gradient near the wedge. Figure 17 also shows the temperature distribution near the wedge (enlarged graph). As appeared in the graph, the temperature gradient near the object surface is steeper than the reference, which leads to the large difference of the heat flux distribution. Indicates that the treatment near the object surface is not accurately enough. Although surface treatment for temperature or wall heat flux should be improved, the temperature distribution in the compression region is expected to be solved accurately. In the future, it will be necessary to review a method to correctly calculate the temperature distribution in the vicinity of the object using IBM.

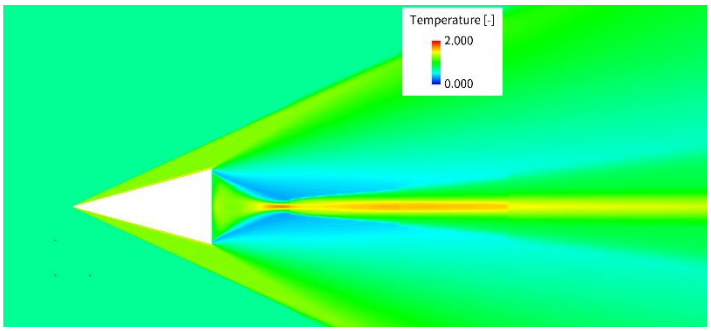

(a) Fine

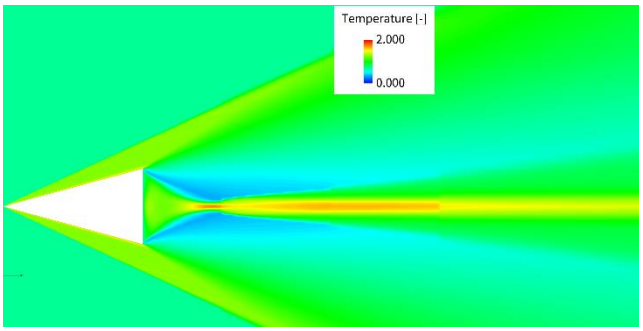

(b) Medium

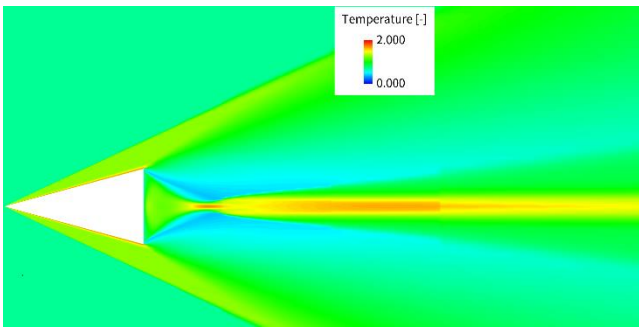

(c) Coarse

Figure 16 Nondimensionalized temperature distribution visualization diagram

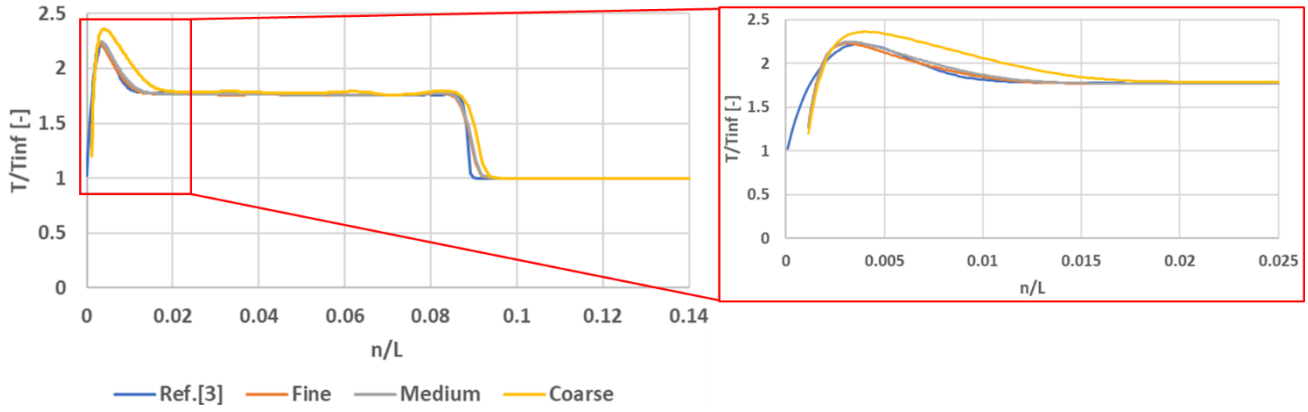

(a)0.5*L*

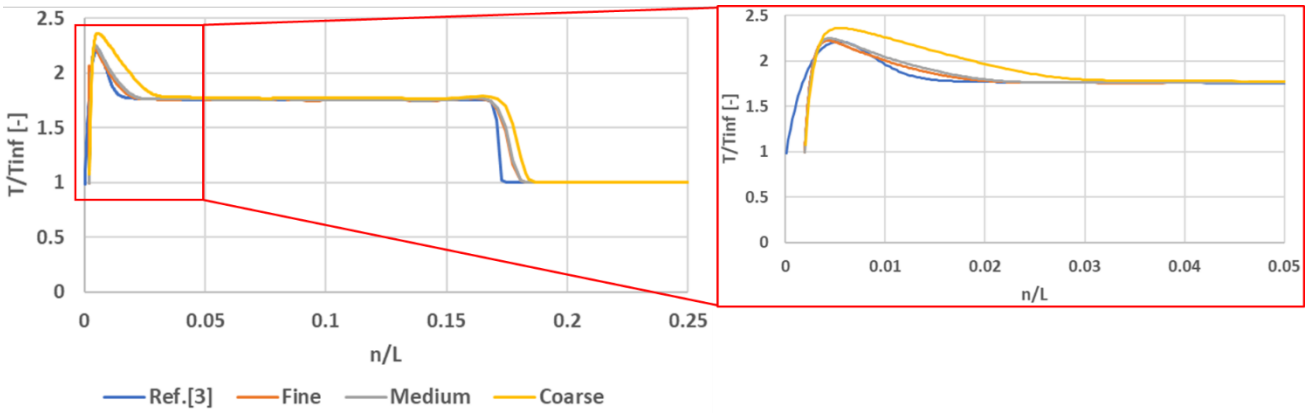

(b)1.0*L*

Figure 17 Temperature distribution

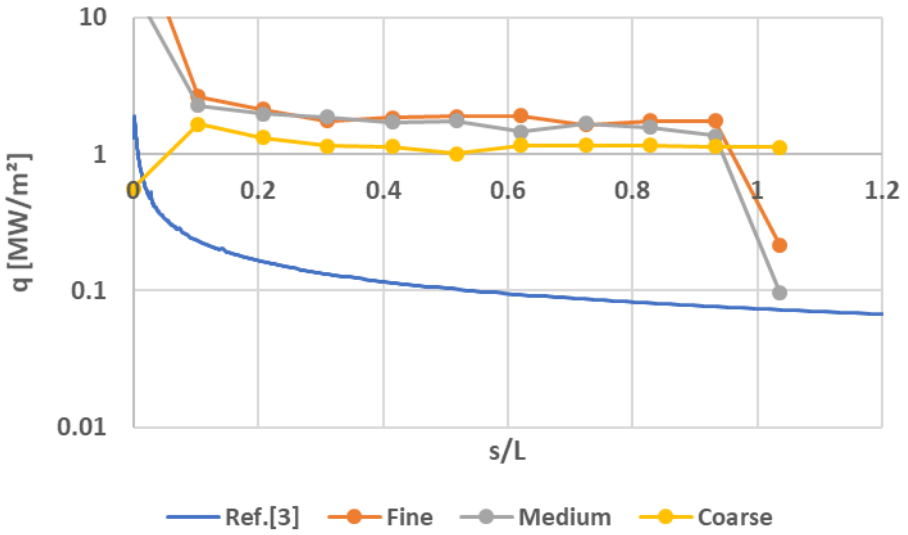

Figure 18 Heat Flux Distribution

5. Conclusion and Future Work

Cartesian-Mesh CFD with revised Immersed Boundary Method for isothermal wall boundary condition is employed to compute supersonic flows around a blunt body (a circular cylinder) and a sharp body (a wedge). The pressure component that included shock waves was in close agreement with the results of the structured mesh. For a case of a cylinder with bow shock, the temperature component, including the heat flux, was predicted precisely to some extent. The comparison of three different mesh resolution confirms that the minimum mesh size or cell Reynolds number can be an indicator for the accurate prediction of the heat flux. In the case of wedge, the temperature distribution in space was precisely predicted, while the temperature distribution near the wedge surface was quite different compared to the structured mesh. This cause the large discrepancy of wall heat flux distribution. In the future, the treatment of temperature near the object surface should be improved for the practical use of Cartesian mesh for supersonic/hypersonic vehicles analysis.

6. Contact Author Email Address

The contact author is Kumpei Abe at Kanazawa Institute of Technology, and the corresponding email address is b1810529@planet.kanazawa-it.ac.jp

References

[1] Takaki, R. Verification of surface distribution prediction accuracy in immersed boundary method. JAXA Special Publication, JAXA-SP-20-006, pp 115-124, 2021 (in Japanese).

[2] Takaki, R, Kawai, S, Fukushima, Y, Tamaki, Y, Tsutsumi, S and Shibata, H. Development of a high-speed and high-precision turbulent flow solver using hierarchical cartesian grids. JAXA Special Publication, JAXA-SP-19-007, pp 165-171, 2020 (in Japanese).

[3] Matsuyama, S. "Reference CFD result", Proceeding of the 1st Workshop on Cartesian Grid-based CFD. JAXA Special Publication, JAXA-SP-20-006, pp 63-76, 2021 (in Japanese).

[4] Nakahashi, K., and Kim, L. S.Building-Cube Method for large=scale high resolution flow computation. 42nd AIAA Aerospace Sciences Meeting and Exhibit, 2004.

[5] Mittal, R., Dong, H., Bozlurttas, M., Najjar, F. M., Vargas, A., and Von Loebbecke, A. A versatile sharp interface immersed boundary method for incompressible flows with complex boundaries. Journal of Computational Physics, Vol.227, pp4825-4852, 2008.

[6] Sugaya, K and Imamura, T. Modification of the Immersed Boundary Method for Improving Drag Prediction Accuracy of NASA-CRM. JAXA Special Publication, JAXA-SP-20-008, pp 149-155, 2021 (in Japanese).

[7] Miyazaki, S. and Sasaki, D. Cartesian Grid-based CFD for Shock/Shock Interference of Two Circular Cylinders. AIAA Paper 2021-2851, 2021.

[8] Sasaki, D and Nakahashi, K. Rapid large-scale cartesian meshing for aerodynamic computations. ICAS Paper 2014-0842, 2014

[9] Brahmachary, S, Natarajan, G, Kulkarni, V, Sahoo, N, Ashok, V and Kumar, V. Role of solution reconstruction in hypersonic viscous computations using a sharp interface immersed boundary method. Physical Review, 2021.

Acknowledgments

We would like to thank Dr. Matsuyama at JAXA for providing the structured-mesh CFD data for comparison. Numerical simulations were performed on the Supercomputer system "AFI-NITY" at the Advanced Fluid Information Research Center, Institute of Fluid Science, Tohoku University. We would like to thank Field View CFD, Inc. for providing Field View, which was used for the visualization in this paper.

Copyright Statement